Point defect engineering of high temperature piezoelectric $BiScO_3$-$PbTiO_3$ for high power operation

E. Berganza, C. Pascual-González[+], H. Amorín, A. Castro, M. Algueró*

Instituto de Ciencia de Materiales de Madrid, CSIC. Cantoblanco, 28049 Madrid, Spain

*Corresponding author: Miguel Algueró (E-mail address: malguero@icmm.csic.es)

[+] Current address: Materials Engineering and Research Institute, Sheffield Hallam University. Howard Street, Sheffield, S1 1WB, UK

ABSTRACT

$BiScO_3$-$PbTiO_3$ is used as a model system of $BiMO_3$-$PbTiO_3$ perovskite solid solutions with enhanced electromechanical response at ferroelectric morphotropic phase boundaries, and high Curie temperature to demonstrate specific point defect engineering for high power operation. The objective is to obtain a range of piezoelectric ceramics comparable to hard $Pb(Zr,Ti)O_3$ materials, optimized for the different applications. In this work, a comprehensive study of Mn substitution for Sc is provided. Care is taken to isolate the effects of the point defects from those of concomitant structural and microstructural changes that have been previously described after MnO_2 addition. Results strongly suggest that Mn substitution results in the formation of (Mn_{Sc}'-$V_O^{\bullet\bullet}$) dipolar complexes that effectively clamp domain walls. This is the same mechanism responsible of hardening in $Pb(Zr,Ti)O_3$. Indeed, $Bi_{0.36}Pb_{0.64}Sc_{0.36-x}Mn_xTi_{0.64}O_3$ with x=0.02 is shown to be a high sensitivity piezoelectric with strongly reduced losses, suitable for high power operation between 200 and 400 ºC.

Keywords: Electroceramics; Perovskites; Piezoelectricity; Morphotropic Phase Boundary; Point defects

1. Introduction

$BiScO_3$-$PbTiO_3$ is the most promising system among perovskite solid solutions with general formula $BiMO_3$-$PbTiO_3$ (where M is a trivalent cation in octahedral coordination) and enhanced electromechanical response at ferroelectric morphotropic phase boundaries (MPBs), which show high Curie temperatures [1-6]. These compounds are being investigated extensively as alternative to state-of-the-art $Pb(Zr,Ti)O_3$ (PZT) for expanding the operation temperature of high sensitivity piezoelectric ceramics beyond 200 ºC, up to 400 ºC [7-9].

The binary system (1-x)$BiScO_3$-x$PbTiO_3$ presents a MPB between ferroelectric polymorphs of rhombohedral *R*3*m* and tetragonal *P*4*mm* symmetry at x~0.64, composition for which the Curie temperature T_C is ≈ 450 ºC, while piezoelectric coefficients d_{33} of ~450 pC N^{-1} are typically achieved after poling [1,2]. This T_C is 100 ºC above that of $Pb(Zr,Ti)O_3$. Likewise d_{33} significantly exceeds the figure of ≈245 pC N^{-1} obtained for ceramics of the latter material at its MPB [10]. Moreover, the charge piezoelectric coefficient is comparable to those of available commercial high sensitivity piezoelectric ceramics of chemically engineered PZT [11].

The very high piezoelectric response of the $Pb(Zr,Ti)O_3$ perovskite solid solution at the MPB is known to result from the presence of an intermediate monoclinic phase with *Cm* space group, which provides a structural bridge between the rhombohedral and tetragonal polymorphs [12], and the occurrence of lattice transverse softening at the monoclinic-tetragonal boundary [13]. This results in very high transverse polarizability and thus, in large shear piezoelectricity that is ultimately responsible of the high effective piezoelectric coefficients obtained. The same mechanism must be operative in $BiScO_3$-$PbTiO_3$, for an analogous monoclinic phase has been described [14,15]. However, this single crystal contribution only account for 1/3 of the total piezoelectric coefficient of PZT ceramics [10].

The additional, actually major contribution to the piezoelectric response is originated from ferroelectric/ferroelastic domain wall movements [10,16]. Indeed, the tailoring of this contribution by point defect (or chemical) engineering of $Pb(Zr,Ti)O_3$ has been key to the success of this material technology, and has enabled the available wide family of high sensitivity piezoelectric ceramics optimized for a range of applications. It is currently acknowledged that the viability of novel materials alternative to PZT, either environmentally friendly ones or piezoelectrics for harsh environments, requires the development of analogous point defect engineering for the different oxide compounds. This has not systematically been addressed for any of the $BiMO_3$-$PbTiO_3$ systems up to now, and it is done here for model $BiScO_3$-$PbTiO_3$.

Roughly speaking, there are two main families of $Pb(Zr,Ti)O_3$ based materials, referred as hard and soft PZTs. The former is characterized by reduced domain wall activity and thus, small dielectric and mechanical losses. Low losses are required for high power applications like ultrasound generation or ultrasonic motors, where heating under operation is an issue [11,16]. Hardening is currently achieved by substitution of trivalent species, such a Fe^{3+} for Ti/Zr^{4+} at the B-site. Oxygen vacancies are created for charge compensation, which associate with the acceptor species forming dipolar defects that electrostatically interact with the spontaneous polarization, effectively clamping the domain walls [17,18]. A similar hardening has been reported for $BiScO_3$-$PbTiO_3$ after MnO_2 addition [19,20].

As a matter of fact, the MnO_2 additive was initially used as an effective means of increasing the resistivity of $BiScO_3$-$PbTiO_3$ ceramics at the targeted operation temperatures, from $\sim 10^8$ and 10^5 up to 10^{10} and 10^7 Ω cm at 300 and 450 ºC, respectively [19]. Piezoelectric high sensitivity materials with stable functionality up to temperatures above 400 ºC were obtained by this procedure [7]. The actual mechanism for the enhanced resistivity was later studied [21]. In this report, Mn was shown to incorporate into the perovskite structure as Mn^{3+} substituting for Sc^{3+} (Mn_{Sc}^{x} in the Kröger-Vink notation). A twofold effect was described: firstly, Mn^{2+} was formed after

trapping of the conduction electrons excited from existing oxygen vacancies; and secondly, this Mn^{2+} associated with oxygen vacancies forming (Mn_{Sc}'-$V_O^{\bullet\bullet}$) dipolar defects, whose presence was confirmed by electron paramagnetic resonance (EPR) spectroscopy in reduced samples. As a result, both the electronic and ionic conductivities were decreased. However, hardening was not observed in this study in contradiction with ref. 19 and 20. It is worth noting that these discrepancies may be attributed to a number of parameters that were not well controlled in the previous studies, such as composition. MnO_2 was used as an additive, and assumed to replace for Ti^{4+} in most of these cases. Segregation of TiO_2 must take place then, but this was not discussed [20]. The location of the specific compositions in the phase diagram was not fixed either, and indeed either a shift towards the rhombohedral side of the MPB [19], or fully tetragonal phases [20] have been reported. Additionally, microstructure was not considered, and materials with very different grain size, actually resulting from contradictory Mn effects, were compared.

In this paper, we report a comprehensive study of the effect of Mn substitution for Sc, rather than using it as an additive, into $BiScO_3$-$PbTiO_3$. Processing was carefully tailored to obtain ceramic materials with comparable microstructure and phases; that is, always at the core of the MPB, with increasing levels of Mn substitution. This allowed the effect of point defects to be isolated from those of grain size and position within the MPB region.

2. Experimental

Dense, highly homogenous ceramic materials were processed from nanocrystalline powders obtained by mechanochemical activation of precursors in a high energy planetary mill. This is a powerful technique for the synthesis of nanocrystalline functional oxides, which allows most known, technologically relevant low tolerance factor perovskite compounds like ferroelectric

$Pb(Zn_{1/3}Nb_{2/3})O_3$ [22], multiferroic $BiFeO_3$ [23], and the ferromagnetic insulator $BiMnO_3$ [24], along with their solid solutions with $PbTiO_3$ [23,25-27] to be obtained at ambient pressure and temperature.

Specifically, perovskite single phase nanocrystalline powders of $Bi_{0.36}Pb_{0.64}Sc_{0.36-x}Mn_xTi_{0.64}O_3$ with x=0, 0.02 and 0.05 were synthesized by mechanochemical activation of stoichiometric mixtures of analytical grade Bi_2O_3 (Aldrich, 99.9% pure), Sc_2O_3 (Aldrich, 99.9% pure), PbO (Merck, 99% pure), TiO_2 (anatase, Cerac, 99% pure) and Mn_2O_3 (Aldrich, 99% pure) with a Pulverisette 6 model Fritsch planetary mill. In all cases, about 10 g of the mixture of the precursor oxides was initially homogenized by hand in an agate mortar, and placed in a tungsten carbide (WC) jar of 250 ml with seven, 2 cm diameter, 63 g mass each WC balls for activation at 300 r.p.m., for 20 h. These conditions have been shown to provide perovskite single phase fully crystalline powders with nanometer-scale chemical homogeneity for the unmodified composition (x=0) [28,29], and were found here to lead to analogous results for the two materials that included an increasing level of Mn substitution. This is illustrated in Fig. 1, where X-ray diffraction (XRD) patterns for the three mechanosynthesized powders are shown. A Bruker D8 Advance diffractometer and Cu Kα radiation (λ=1.5418 Å) were used for the measurements, for which a 0.1º (2θ) step and 1.5 s counting rate were selected. Crystallite size was obtained from the XRD data by using the Scherrer equation [30], and ranged between 12 and 16 nm with no systematic trend with Mn level. The powder nanocrystalline nature was confirmed by transmission electron microscopy (JEM 2000FXII microscope working at 200 keV). TEM images of the sample with x=0.02 are also included in the Figure as an example.

Ceramic processing was carried out by conventional means. About 1 g of nanocrystalline powder was uniaxially pressed into 12 mm diameter pellets, which were then sintered in a closed Al_2O_3 crucible inside a furnace. A temperature of 1100 ºC, a soaking time of 1 h and heating/cooling rates of ± 3 ºC min^{-1} were selected. Note that significant PbO or Bi_2O_3 losses did

not take place under these conditions, as checked by monitoring weight changes during sintering. This is thought to be a characteristic of the perovskite nanocrystalline powders obtained by mechanosynthesis, which are fully crystallized after the mechanical treatment, and do not require any subsequent calcination step. Note that traces of PbO contamination on the crucible inner walls were not found at the sintering temperature used. Negligible losses allowed the use of initial precursor excesses or of sacrificial powder; that is, to bury the green bodies in powder during the thermal treatment, to be avoided. This highly facilitates composition and phase coexistence control, a crucial factor in this work. Densification values above 95% were consistently achieved.

Samples for phase and microstructural characterizations were prepared by thinning of ceramics to remove a surface layer (~100 μm), followed by polishing to a mirror finish. The thinning step was introduced to get rid of any hypothetical surface layer with slightly deviated composition, caused by unnoticed PbO or Bi_2O_3 losses (involving weight changes below the sensitivity of the mass measurement). A final thermal treatment at 600 ºC for 2 h with ± 0.5 ºC min^{-1} was carried out to remove the damage introduced, and to restore the equilibrium polymorphic phase coexistence and domain configurations, which are modified by the shear stresses involved in polishing [31].

Perovskite phase stability during sintering was controlled by XRD with a Siemens D500 powder diffractometer and Cu K_α radiation. Patterns were recorded between 20 and 50º (2θ) with 0.05º (2θ) step and 5 s counting rate. Slow scans; 0.02º (2θ) step and 10 s counting rate, were carried out between 43 and 47º (2θ) across the perovskite parent cubic phase 200 diffraction peak, for the analysis of the ferroelectric distortion and the evaluation of the phase percentages within the phase coexistence region.

Microstructure was studied with a FEI Nova™ NanoSEM 230 field emission gun scanning electron microscope equipped with an Oxford INCA 250 electron dispersive X-ray spectrometer for chemical analysis.

Ceramic capacitor for electrical and electromechanical characterizations were prepared by thinning discs down 0.5 mm, painting Ag electrodes on the major faces, and sintering them at 700 ºC.

Electrical characterization started by evaluating the total dc conductivity, along with its bulk and grain boundary components by impedance spectroscopy analysis. Data were recorded in static conditions, from 250 to 550 ºC, at 20 ºC intervals, in the 20 Hz - 1 MHz range with a HP4284A precision LCR meter. The Z-view2 commercial software was used for the analysis.

Dielectric permittivity and ferroelectric hysteresis loops were characterized in a second stage. Dependences of the dielectric permittivity and losses on temperature were measured between room temperature (RT) and 550 ºC with the same HP4284A precision LCR meter. Measurements in this case were dynamically carried out during a heating/cooling cycle with $\pm$1.5 ºC min^{-1} rate at several frequencies between 100 Hz and 1 MHz. RT ferroelectric hysteresis loops were recorded under voltage sine waves of increasing amplitude up to 10 kV with a 0.1 Hz frequency, obtained by the combination of a synthesizer/function generator (HP 3325B) and a high voltage amplifier (TREK model 10/40), while charge was measured with a homebuilt charge-to-voltage converter and software for loop acquisition and analysis.

Finally, the ceramic discs were poled for electromechanical characterization. A field of 4 kV mm^{-1} was applied at 100 ºC for 15 min, and maintained during cooling down to 40 ºC. These are standard conditions for the poling of $BiScO_3$-$PbTiO_3$ ceramics [1,2,5]. The longitudinal piezoelectric coefficient d_{33} was then measured 24 h after the poling step with a Berlincourt type meter. Also, the transverse piezoelectric coefficient was obtained by complex analysis of

piezoelectric radial resonances of the discs by an automatic iterative method described elsewhere [32]. This procedure also provides the s_{11}^E and s_{12}^E compliances and ε_{33}^σ permittivity of the poled material all in complex form and thus, all mechanical, electrical and electromechanical losses.

3. Results and discussion

XRD patterns for $Bi_{0.36}Pb_{0.64}Sc_{0.36-x}Mn_xTi_{0.64}O_3$ with x=0, 0.02 and 0.05 are shown in Fig. 2. No secondary phases in addition to the perovskite one are found in any of the ceramics processed with increasing levels of Mn substitution, suggesting that the targeted incorporation of the new atomic species into the structure has been achieved.

Patterns with improved statistics across the perovskite parent cubic phase 200 diffraction peak, along with their deconvolution by using three pseudo-Vöigt functions are given in Fig. 3. The coexistence of rhombohedral and tetragonal phases is assumed for simplicity, even though the former polymorph is likely to be monoclinic, according to previous reports. However, an analysis with four peaks is beyond the capabilities of the lab-scale XRD equipment and out of the scope of this work. Even with this limitation, results clearly indicate all materials with increasing amount of Mn to remain within the morphotropic phase boundary region. Indeed, the percentage of rhombohedral and tetragonal phases does not change significantly after substitution with x=0.02, the only effect being a small shift of all peaks towards higher angles. This indicates some cell shrinkage, which was expected from the ionic radii differences for sixfold coordination of Sc^{3+} and Mn^{3+} that are 0.745 Å and 0.58/0.645 Å (low/high spin configurations), respectively [33]. Larger shifts are found after substitution with x=0.05, which also results in a slight increase of the

amount of rhombohedral phase, yet still in coexistence with the tetragonal phase, which shows a decreased tetragonal distortion.

Scanning electron microscopy (SEM) images of the polished surfaces of the three ceramics with increasing amounts of Mn are shown in Fig. 4. Homogenous microstructures with average grain sizes of 2.4, 1.7 and 2.3 μm for x=0, 0.02 and 0.05, respectively, were obtained. No significant microstructural changes are thus induced by the Mn substitution.

The preliminary characterization confirms that this series of materials is ideally suited to study the effect of the introduction of Mn_{Sc}^{x} point defects on properties, avoiding ambiguities arising from concomitant phase or microstructural effects. Indeed, it is somehow surprising that Mn substitution for Sc did not modify microstructure or phase coexistence, unlike in previous reports where MnO_2 was used as an additive during sintering. In those works, all starting from powders obtained by conventional solid state synthesis, the manganese oxide addition caused grain coarsening, with average values that increased from 1.3 to 8.9 μm [21], or from 3 to 8-10 μm [20]. It must be noted though that a grain size of 7.5 μm has also been reported for ceramics processed without MnO_2 additive with the same sintering temperature of 1100 ºC (increased up to 15 μm for 1150 ºC) [1].

In order to investigate the origin of these discrepancies, we tailored the processing to obtain ceramics with increased grain size. This was achieved by using powders arrested at an intermediate stage of the mechanosynthesis (15 h), and by processing the ceramics at 1125 ºC (1150 ºC was also tested but resulted in poor dielectric strength). A SEM image of such ceramic with x=0.02 is shown in Fig. 5, along with its XRD pattern. No secondary phases are found in XRD, though a liquid phase is clearly observed at triple points and grain boundaries in SEM (see arrow). This suggests the occurrence of exaggerated grain growth, and indeed an average grain size of 9 μm resulted. Note also the clear shift of the phase coexistence towards the tetragonal

side of the MPB region, in agreement with [20], but not with [19]. Similar phase deviation during liquid phase sintering has been described for $Pb(Mg_{1/3}Nb_{2/3})O_3$-$PbTiO_3$ [34], illustrating the difficulties in controlling the sample characteristics once this grain growth mode is triggered. Nevertheless, this sample was also fully characterized along with the series of ceramics with fine grained microstructure to facilitate comparison with the mentioned previous reports.

A key issue in this study is the effective incorporation of Mn into the perovskite, avoiding the segregation of manganese oxides at the grain boundaries. This incorporation is clearly indicated by changes in conductivity after Mn substitution. Fig. 6 shows the Arrhenius plots for the total *dc* conductivity of the series of ceramics with an increasing level of Mn. All materials show a common high temperature regime characterized by an activation energy ranging from 1.1 to 1.2 eV. This figure is typical of the electromigration of mobile doubly ionized oxygen vacancies $V_O^{\bullet\bullet}$ and thus, one can assume ionic conductivity to dominate the electrical response above 400 ºC [35]. A distinctive decrease of conductivity takes place in this regime after Mn substitution. This effect has already been described, and associated with the formation of Mn_{Sc}', and its association with oxygen vacancies to form (Mn_{Sc}'-$V_O^{\bullet\bullet}$) dipolar complexes that effectively pin the ionic charge carriers [21].

Additionally, novel conduction phenomena are found below 400 ºC that have not been discussed before. In the case of the ceramic materials without Mn substitution (x=0), the temperature dependence of conductivity shows a distinctive change of slope at ~450 ºC, below which the activation energy increases up to 1.6 eV. This temperature corresponds to the ferroelectric transition, at which ferroelectric domains develop. Assuming oxygen vacancies to be still the charge carriers, it is suggested that the increase of activation energy might be associated with domain walls being an obstacle to the movement of the oxygen vacancies.

A very different behavior is found for the materials with Mn substitution (x=0.02 and 0.05). A change of slope is also observed, but indicating in this case a decrease of activation energy down to 0.65 eV. This figure is typical of electronic conduction rather than ionic, and it is proposed to be associated with hole conduction within the valence band, specifically with electron hopping between Mn^{2+} and Mn^{3+} at the B-site. Indeed, a similar conduction process has been described for $BiScO_3$-$PbTiO_3$ ceramics processed from powder synthesized by mechanochemical activation in stainless steel media [36], for which presence of Fe substituting for Sc has been described [5].

Impedance spectroscopy analysis was used to isolate bulk (or grain bulk) and grain boundary contributions to the total electrical response, and to confirm that Mn effects on conductivity were truly bulk effects, and not grain boundary ones. Data were initially analyzed using the electric modulus formalism, which allowed two Debye-like relaxation processes to be readily identified for all materials with increasing content of Mn. This indicates the presence of two electroactive regions that are associated with the grain bulk (low frequency process) and the grain boundaries (high frequency process). A similar result has been shown for closely related $BiScO_3$-$PbTiO_3$ materials [36]. The contributions of the two regions were separated by using an equivalent electric circuit to model the experimental data. A series connection of two parallel (RQC) and (RQ) elements for the bulk and grain boundary components, respectively, was used that has been previously shown to correctly model the response of $BiScO_3$-$PbTiO_3$ ceramics [36]. Results for samples with x=0.02 are given in the Figure. Note that the low temperature electronic process associated with hopping between Mn^{2+} - Mn^{3+} species at the *B*-site of the perovskite is observed in the bulk component. This confirms the correct incorporation of Mn into the perovskite.

Results for the ceramic with a coarsened microstructure and phase coexistence shifted towards the tetragonal side are also included. The main features of conductivity behaviour discussed above are reproduced, indicating that exaggerated grain growth does not result in Mn segregating at grain boundaries.

The presence of oxygen vacancies for all samples was also indicated by the high temperature dielectric response. Temperature dependences of the relative permittivity and loss tangent for the three ceramic materials with an increasing level of Mn substitution are shown in Figs. 7 and 8 at several frequencies between 100 kHz and 1 MHz. Only the cooling half-cycle is given for clarity. Strong low-frequency dispersion was found across the temperature range where the ferroelectric transition takes place in all cases. This type of high temperature Debye type relaxation processes are usually attributed to point defects like the oxygen vacancies already revealed by the conductivity results [35].

High temperature dielectric relaxations complicate the accurate determination of the ferroelectric transition temperatures from the associated dielectric anomalies. This was done by using the curves at 1 MHz, for which relaxations have already shifted well above the temperature range of interest (see Figure 8). Mn incorporation into the bulk perovskite resulted in the gradual decrease of the ferroelectric transition temperature. This shift is illustrated in Fig. 9, where the temperature dependence of permittivity is shown for the three ceramics during a full heating/cooling cycle from RT up to 550 ºC. The dielectric anomaly associated with the transition is observed at a temperature of 450, 435 and 420 ºC for x=0, 0.02 and 0.05, respectively. Besides, a distinctive decrease of the RT dielectric permittivity and losses of the unpoled ceramics is also found with increasing Mn content. Exaggerated grain growth does not modify the position of the ferroelectric transition (see Figure), but results in an increased permittivity, so as the ceramic material with x=0.02 and a grain size of 9 μm has a permittivity larger than the fine grained material with x=0. Values are given in Table 1, along with the T_Cs. This phenomenology nicely illustrates the necessity of controlling microstructure when studying the effect of point defects.

Ferroelectric hysteresis loops for all materials are shown in Fig. 10. Note the distinctive increase of coercive field, from 2.5 up to 3.5 kV mm^{-1}, when a Mn content of x=0.02 is introduced.

This takes place in two ceramics with very similar grain size and phase coexistence, so it is a direct evidence of domain wall mobility being reduced after Mn substitution. Exaggerated grain growth in this case decreases the coercive field down to 2.6 kV mm^{-1}, which is the value obtained for the fine grained unmodified material. There is thus a strong effect of grain size on coercive field, which reflects changes in the domain configuration and an increasing influence of low permittivity grain boundaries [36]. Whatever the cause is, grain size effects may hide the effect of point defects. This is most probably the reason why several previous reports on Mn substituted $BiScO_3$-$PbTiO_3$ concluded that hardening was absent.

It is surprising the strong depletion of the ferroelectric switching characteristics for the ceramic with x=0.05, which has a low remnant polarization of 13 $\mu C\ cm^{-2}$, as compared with 40 and 36 $\mu C\ cm^{-2}$ for those with x=0 and 0.02, respectively. Its lean character is typical of materials with frozen strain or/and compositional gradients, which might be also responsible of the smaller tetragonal distortion found. Besides, this could explain why conductivity values hardly change from x=0.02 to 0.05. The material with x=0.05 is thus assumed to be inhomogeneous; most probably regarding Mn substitution, and for that reason the following discussion on the effects of point defects is mostly focused in x=0.02.

Charge longitudinal piezoelectric coefficient d_{33} values after poling are given in Table 1. There is a continuous decrease with x, from 440 down to 250 and 210 pC N^{-1} for x=0, 0.02 and 0.05, respectively. Piezoelectric radial resonances are shown in Fig. 11 for the materials with x=0 and 0.02. Note the significant narrowing of the resonances after Mn addition (also observed for x=0.05, not shown, and related to an increase of the mechanical quality factors Q_s and Q_p from 20 and 45 to 235 and 400). Complex material coefficients obtained from the analysis of these resonances are given in Table 1. All the d_{31} piezoelectric coefficient, s_{11}^E and s_{12}^E compliances, and ε_{33}^σ permittivity decrease with x, along with all losses, either dielectric, mechanical or

electromechanical from values of 0.096, 0.05 and 0.1 down to 0.014, 0.009 and 0.01, respectively, when a Mn level of x=0.02 is substituted, while microstructure remains similar. A slight broadening of the piezoelectric resonance takes place after exaggerated grain growth for x=0.02, though the mechanical quality factor does not return to the values of the unmodified material, like do not all coefficient and losses.

These results unambiguously demonstrate that the introduction of Mn substituting for Sc in high temperature piezoelectric $BiScO_3$-$PbTiO_3$ is an effective means of reducing domain wall mobility. The previously reported decrease of high temperature ionic conductivity is confirmed, though an additional electronic component appears after Mn substitution that dominates the response below 350 ºC. Therefore, conductivity is not effectively reduced below this temperature, though conductivity values are never an issue for operation. Indeed, the Mn substituted $BiScO_3$-$PbTiO_3$ fine grained ceramics are high sensitivity piezoelectrics with strongly reduced losses and high Curie temperature.

4. Summary and conclusions

We have succeeded in processing, using chemically homogenous nanocrystalline powders obtained by mechanosynthesis, a series of fine grained piezoelectric ceramics of $BScO_3$-$PbTiO_3$ with increasing levels of Mn substituting for Sc, and controlled grain size and phase coexistence, ideally suited to establish the effect of the introduced point defects in properties. The correct incorporation of Mn into the B-site of the perovskite structure is indicated by the results. Conductivity changes strongly suggest the formation of Mn_{Sc}', and its association with existing oxygen vacancies to form (Mn_{Sc}'-$V_O^{\bullet\bullet}$) dipolar complexes. The ferroelectric hysteresis loops and the linear coefficients; permittivity, compliances and piezoelectric coefficients, along with their

associated losses, all reflect a distinctive decrease of the ferroelectric domain wall activity with Mn substitution. This is consistent with the presence of the mentioned dipolar complexes, which has been experimentally proved by EPR in ref. 21. Overall, Mn substituted $BiScO_3$-$PbTiO_3$ is a hard material with a Curie temperature of 435 ºC, and a d_{33} coefficient of 250 pC N^{-1} that can be enhanced up to 310 pC N^{-1} by microstructure coarsening, while maintaining strongly reduced losses. This is thus a first step towards the development of specific point defect engineering for BMO_3-$PbTiO_3$ systems comparable to that of PZT.

Acknowledgements

Funded by Spanish MINECO through the MAT2014-58816-R and MAT2011-23709 projects. Technical supports by Ms. I. Martínez and Ms. M. M. Antón are also acknowledged.

References

[1] R.E. Eitel, C.A. Randall, T.R. Shrout, S.E. Park, Preparation and characterization of high temperature perovskite ferroelectrics in the solid-solution (1-x)$BiScO_3$-x$PbTiO_3$, Jpn. J. Appl. Phys. 41 (2002) 2099-2104.

[2] R.E. Eitel, S.J. Zhang, T.R. Shrout, C.A. Randall, I. Levin, Phase diagram of the perovskite system (1-x)$BiScO_3$-x$PbTiO_3$, J. Appl. Phys. 96 (2004) 2828-2831.

[3] T. Zou, X. Wang, H. Wang, C. Zhong, L. Li, I.W. Chen, Bulk dense fine-grain (1−x)$BiScO_3$–x$PbTiO_3$ ceramics with high piezoelectric coefficient, Appl. Phys. Lett. 93 (2008) art. nº 192913.

[4] A. Sehirlioglu, A. Sayir, F. Dynys, Doping of $BiScO_3$-$PbTiO_3$ ceramics for enhanced properties, J. Am. Ceram. Soc. 93 (2010) 1718-1724.

[5] M. Alguero, P. Ramos, R. Jiménez, H. Amorín, E. Vila, A. Castro, High temperature piezoelectric $BiScO_3$-$PbTiO_3$ synthesized by mechanochemical methods, Acta Mater. 60 (2012) 1174-1183.

[6] J.G. Chen, G.X. Jin, C.M. Wang, J.R. Cheng, Reduced dielectric loss and strain hysteresis in Fe and Mn comodified high-temperature $BiScO_3$-$PbTiO_3$ ceramics, J. Am. Ceram. Soc. 97 (2014) 3890-3896.

[7] S. Zhang, R.E. Eitel, C.A. Randall, T.R. Shrout, E.F. Alberta, Manganese-modified $BiScO_3$–$PbTiO_3$ piezoelectric ceramic for high-temperature shear mode sensor, Appl. Phys. Lett. 86 (2005) art. nº 262904.

[8] A. Sehirlioglu, A. Sayir, F. Dynys, High temperature properties of $BiScO_3$–$PbTiO_3$ piezoelectric ceramics, J. Appl. Phys. 106 (2009) art. nº 014102.

[9] J. Chen, Z. Chen, X. Li, S. Dong, A high-temperature piezoelectric linear actuator operating in two orthogonal first bending modes, Appl. Phys. Lett. 102 (2013) art. nº 052902.

[10] Q.M. Zhang, H. Wang, N. Kim, L.E. Cross, Direct evaluation of domain-wall and intrinsic contributions to the dielectric and piezoelectric response and their temperature dependence on lead zirconate-titanate ceramics, J. Appl. Phys. 75 (1994) 454-459.

[11] K. Uchino, Materials issues in design and performance of piezoelectric actuators: An overview, Acta Mater. 46 (1998) 3745-3753.

[12] B. Noheda, J.A. Gonzalo, L.E. Cross, R. Guo, S.E. Park, D. Cox, G. Shirane, Tetragonal-to-monoclinic phase transition in a ferroelectric perovskite: The structure of $PbZr_{0.52}Ti_{0.48}O_3$, Phys. Rev. B 61 (2000) 8687-8695.

[13] D. Damjanovic, Comments on origins of enhanced piezoelectric properties in ferroelectrics, IEEE Trans. Ultrason. Ferroel. Freq. Control 56 (2009) 1574-1585.

[14] J. Chaigneau, J.M. Kiat, C. Malibert, C. Bogicevic, Morphotropic phase boundaries in $(BiScO_3)_{1-x}(PbTiO_3)_x$ ($0.60 < x < 0.75$) and their relation to chemical composition and polar order, Phys. Rev. B 76 (2007) art. nº 094111.

[15] T. Hungría, F. Houdellier, M. Alguero, A. Castro, Monoclinic symmetry of twin-free nanocrystals in the $BiScO_3$-$PbTiO_3$ solid solution as revealed by aberration-corrected TEM, Phys. Rev. B 81 (2010) art. nº 100102(R).

[16] D. Damjanovic, Ferroelectric, dielectric and piezoelectric properties of ferroelectric thin films and ceramics, Rep. Prog. Phys. 61 (1998) 1267-1324.

[17] U. Robels, G. Arlt, Domain wall clamping in ferroelectrics by orientation of defects, J. Appl. Phys. 73 (1993) 3454-3460.

[18] M.I. Morozov, D. Damjanovic, Charge migration in $Pb(Zr,Ti)O_3$ ceramics and its relation to ageing, hardening, and softening, J. Appl. Phys. 107 (2010) art. nº 034106.

[19] S.J. Zhang, E.F. Alberta, R.E. Eitel, C.A. Randall, T.R. Shrout, Elastic, piezoelectric, and dielectric characterization of modified $BiScO_3$-$PbTiO_3$ ceramics, IEEE Trans. Ultrason. Ferroelectr. Freq. Control 52 (2005) 2131-2139.

[20] J. Chen, Z. Hu, H. Shi, M. Li, S. Dong, High-power piezoelectric characteristics of manganese-modified $BiScO_3$-$PbTiO_3$ high-temperature piezoelectric ceramics, J. Phys D: Appl. Phys. 45 (2012) art. nº 465303.

[21] M.D. Drahus, P. Jakes, E. Erdem, S. Schaab, J. Chen, M. Ozerov, S. Zvyagin, R.A. Eichel, Manganese-doped (1-x)$BiScO_3$-x$PbTiO_3$ high-temperature ferroelectrics: Defect structure and mechanism of enhanced electric resistivity, Phys. Rev. B 84 (2011) art. nº 064113.

[22] J. Wang, D.M. Wan, J.M. Xue, W.B. Ng, Synthesizing nanocrystalline $Pb(Zn_{1/3}Nb_{2/3})O_3$ powders from mixed oxides, J. Am. Ceram. Soc. 82 (1999) 477-479.

[23] C. Correas, T. Hungria, A. Castro, Mechanosynthesis of the whole x$BiFeO_3$-(1-x)$PbTiO_3$ multiferroic system: structural characterization and study of phase transitions, J. Mater. Chem. 21 (2011) 3125-3132.

[24] A. Castro, C. Correas, O. Peña, A.R. Landa-Canovas, M. Alguero, H. Amorin, M. Dolle, E. Vila, T. Hungria, Nanostructured $BiMnO_{3+\delta}$ obtained at ambient pressure: analysis of its multiferroicity, J. Mater. Chem. 22 (2012) 9928-9938.

[25] M. Alguero, J. Ricote, A. Castro, Mechanosynthesis and thermal stability of piezoelectric perovskite 0.92$Pb(Zn_{1/3}Nb_{2/3})O_3$-0.08$PbTiO_3$ powders, J. Am. Ceram. Soc. 87 (2004): 772-778.

[26] T. Hungria, C. Correas, F. Houdellier, O. Peña, E. Vila, A. Castro, Study of nanocrystalline $BiMnO_3$--$PbTiO_3$: Synthesis, structural elucidation, and magnetic characterization of the whole solid solution, Chem. Eur. J. 18 (2012) 9075-9082.

[27] C.M. Fernandez-Posada, H. Amorin, C. Correas, O. Peña, M. Alguero, A. Castro, Mechanosynthesis and multiferroic properties of the $BiFeO_3$-$BiMnO_3$-$PbTiO_3$ ternary system along its morphotropic phase boundary, J. Mater. Chem. C 3 (2015) 2255-2265.

[28] M. Alguero, J. Ricote, T. Hungria, A. Castro, High-sensitivity piezoelectric, low-tolerance-factor perovskites by mechanosynthesis, Chem. Mater. 19 (2007) 4982-4990.

[29] H. Amorin, T. Hungria, A.R. Landa-Canovas, M. Torres, M. Dolle, M. Alguero, A. Castro, Nanopowders of ferroic oxides for magnetoelectric composites, J. Nanopart. Res. 13 (2011) 4189-4200.

[30] B.D. Cullity, *Elements of X-ray Diffraction*, Series in Metallurgy and Materials, Addison-Wesley, Reading, MA (1967).

[31] M.F. Wong, K. Zeng, Mechanical polishing effects toward surface domain evolution in $Pb(Zn_{1/3}Nb_{2/3})O_3$-$PbTiO_3$ single crystals, J. Am. Ceram. Soc. 94 (2011) 1079-1086.

[32] C. Alemany, A.M. Gonzalez, L. Pardo, B. Jimenez, F. Carmona, J. Mendiola, Automatic-determination of complex constants of piezoelectric lossy materials in the radial mode, J. Phys. D: Appl. Phys. 28 (1995) 945-956.

[33] R.D. Shannon, Revised effective ionic-radii and systematic studies on interatomic distances in halides and chalcogenides, Acta Crystallogr. Sect. A 32 (1976) 751-767.

[34] H. Amorin, J. Ricote, J. Holc, M. Kosec, M. Alguero, Homogeneous templated grain growth of $0.65Pb(Mg_{1/3}Nb_{2/3})O_3$-$0.35PbTiO_3$ from nanocrystalline powders obtained by mechanochemical activation, J. Eur. Ceram. Soc. 28 (2008) 2755-2763.

[35] C. Ang, Z. Yu, L.E. Cross, Oxygen-vacancy-related low-frequency dielectric relaxation and electrical conduction in Bi : $SrTiO_3$, Phys. Rev. B 62 (2000) 228-236.

[36] H. Amorin, R. Jimenez, M. Deluca, J. Ricote, T. Hungria, A. Castro, M. Alguero, Nanostructuring effects in piezoelectric $BiScO_3$-$PbTiO_3$ ceramics, J. Am. Ceram. Soc. 97 (2014) 2802-2809.

Table 1 Curie temperatures and material coefficients for the $Bi_{0.36}Pb_{0.64}Sc_{0.36-x}Mn_xTi_{0.64}O_3$ ceramics with x=0, 0.02 and 0.05.

	$\varepsilon_{33}^{\sigma}$ ($x\varepsilon_o$) Unpoled	*Tan* δ Unpoled	T_C (ºC)	d_{33} (pC N^{-1})	d_{31} (pC N^{-1})	$\varepsilon_{33}^{\sigma}$ ($x\varepsilon_o$) Poled	s_{11}^E ($x10^{-12}$ m^2 N^{-1})	s_{12}^E ($x10^{-12}$ m^2 N^{-1})
x=0	835	0.095	450	440	-144+15i	1486-143i	13.8-0.7i	-3.6+0.2i
x=0.02	820	0.055	435	250	-83+i	1153-16i	11.3-0.1i	-3.4
x=0.05	730	0.025	420	210	-76+i	935-12i	10.6	-3.0
x=0.02 EGG	1045	0.050	435	310	-83+3i	978-27i	12.1-0.1i	-4.0

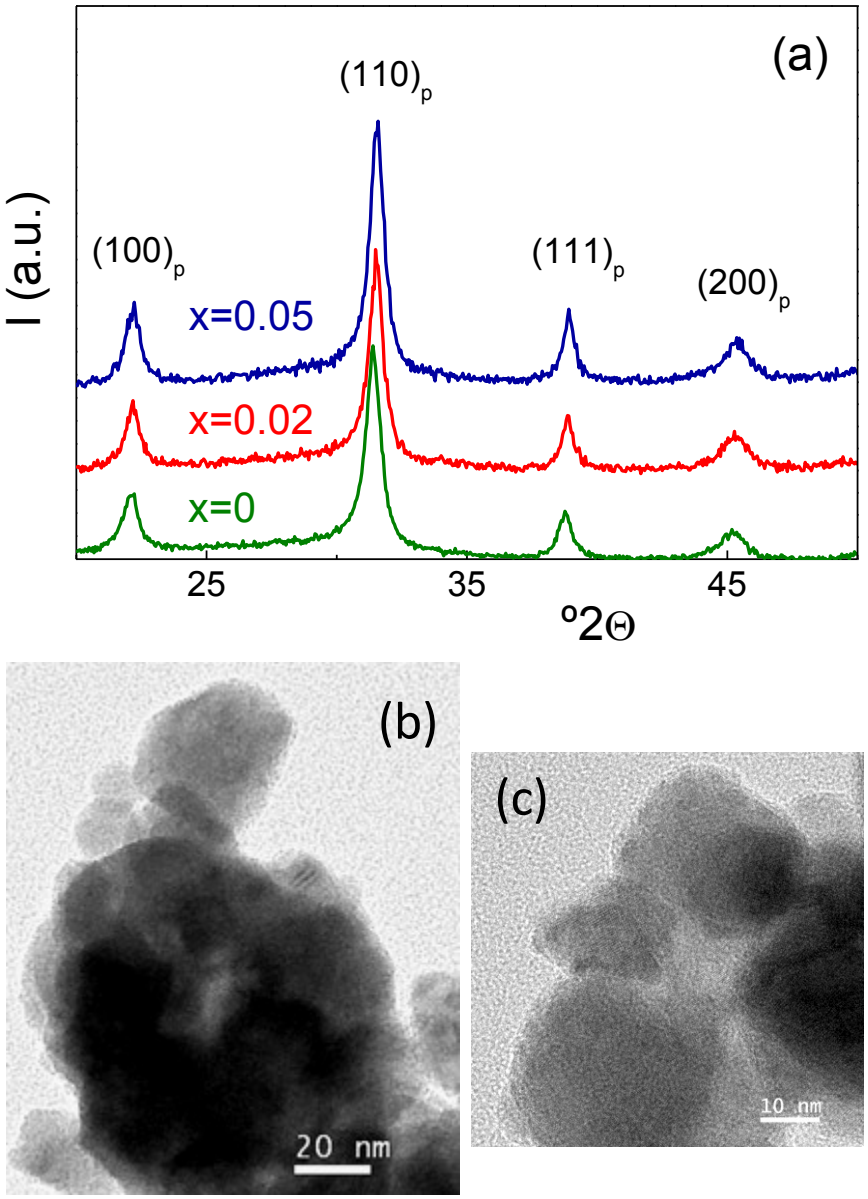

Fig. 1. (a) XRD patterns of the nanocrystalline $Bi_{0.36}Pb_{0.64}Sc_{0.36-x}Mn_xTi_{0.64}O_3$ powders with x=0, 0.02 and 0.05, obtained by mechanosynthesis, and (b,c) TEM images of that with x=0.02.

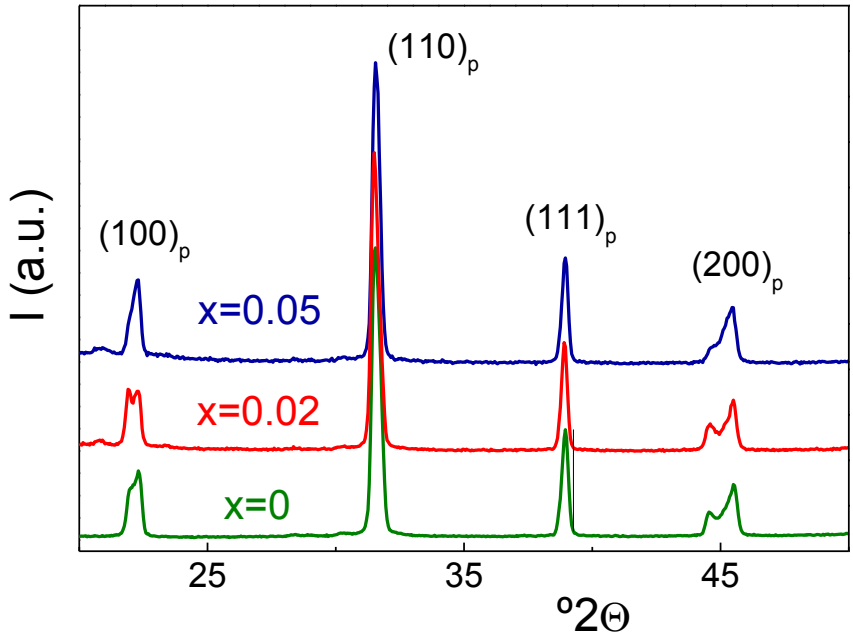

Fig. 2. XRD patterns of $Bi_{0.36}Pb_{0.64}Sc_{0.36-x}Mn_xTi_{0.64}O_3$ ceramics with x=0, 0.02 and 0.05, showing the absence of second phases other than perovskite.

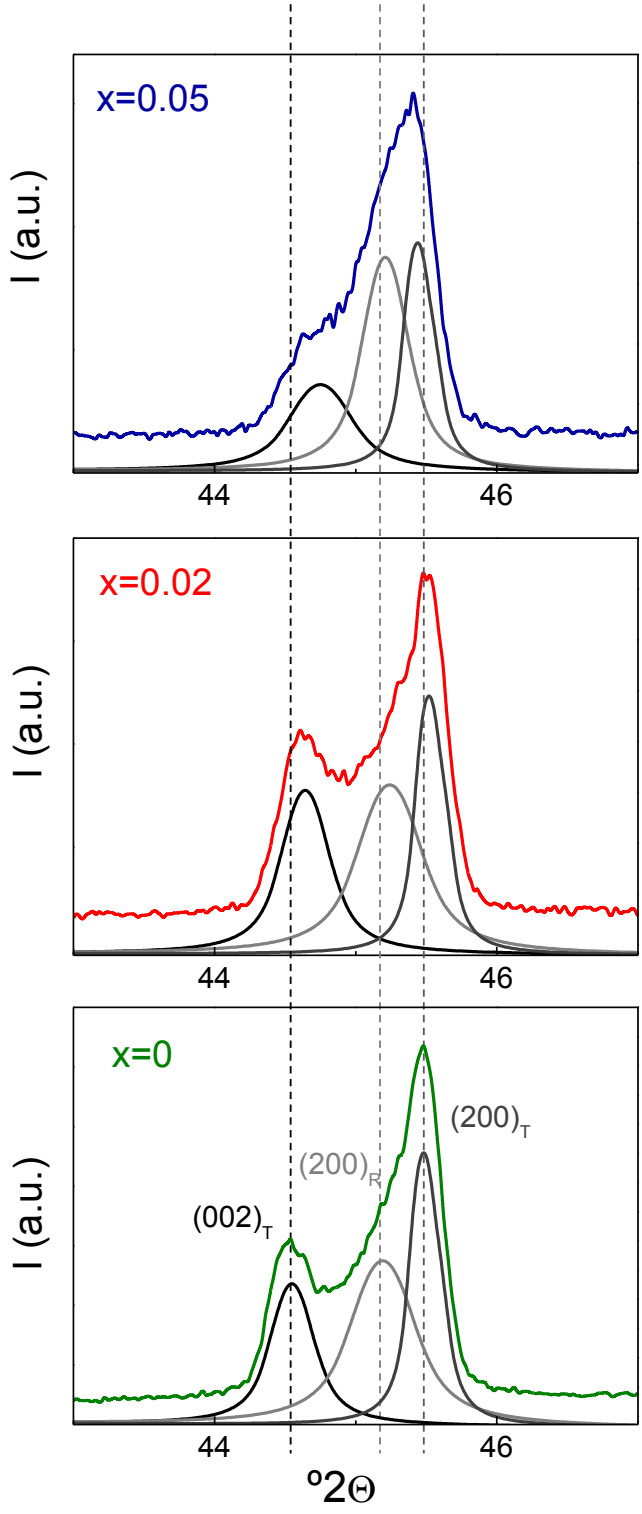

Fig. 3. XRD patterns with improved statistics across the perovskite parent cubic phase 200 diffraction peak of $Bi_{0.36}Pb_{0.64}Sc_{0.36-x}Mn_xTi_{0.64}O_3$ ceramics with x=0, 0.02 and 0.05, showing polymorphic phase coexistence and thus, location of materials at the MPB. T and R in Miller indices stand for the tetragonal and rhombohedral symmetries, respectively.

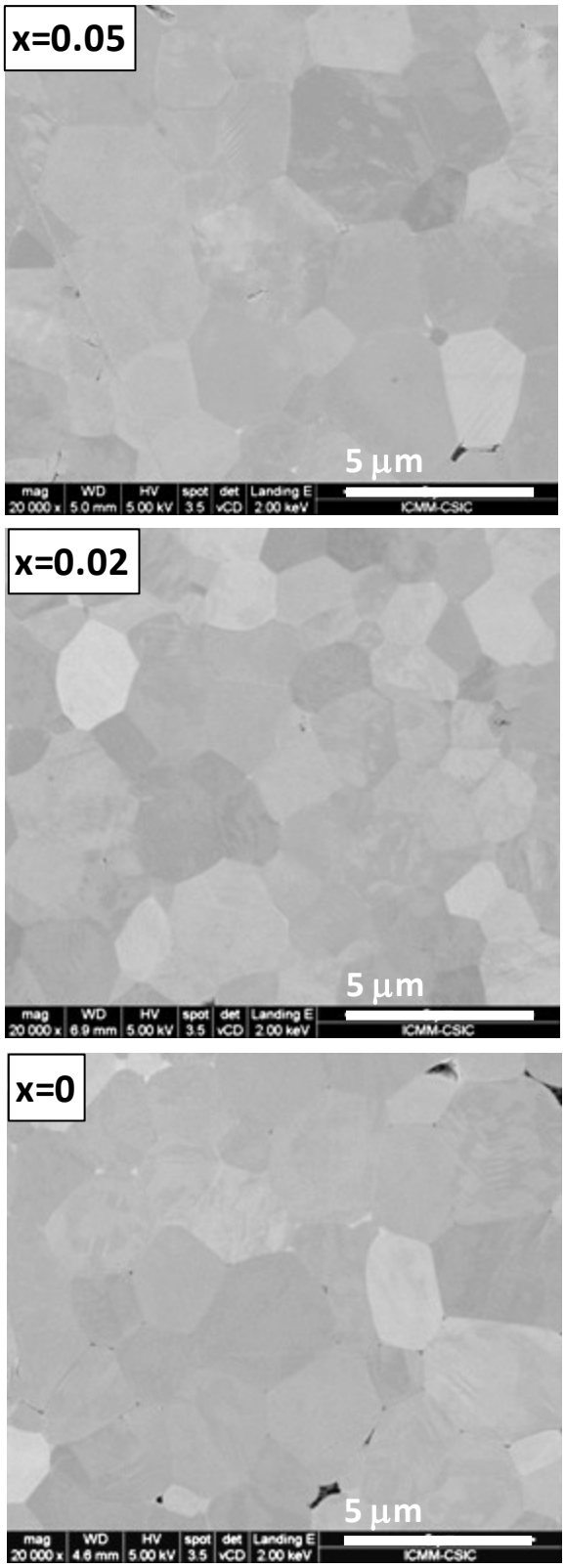

Fig. 4. SEM images of $Bi_{0.36}Pb_{0.64}Sc_{0.36-x}Mn_xTi_{0.64}O_3$ ceramics with x=0, 0.02 and 0.05, showing the dense and homogenous fine-grained microstructures.

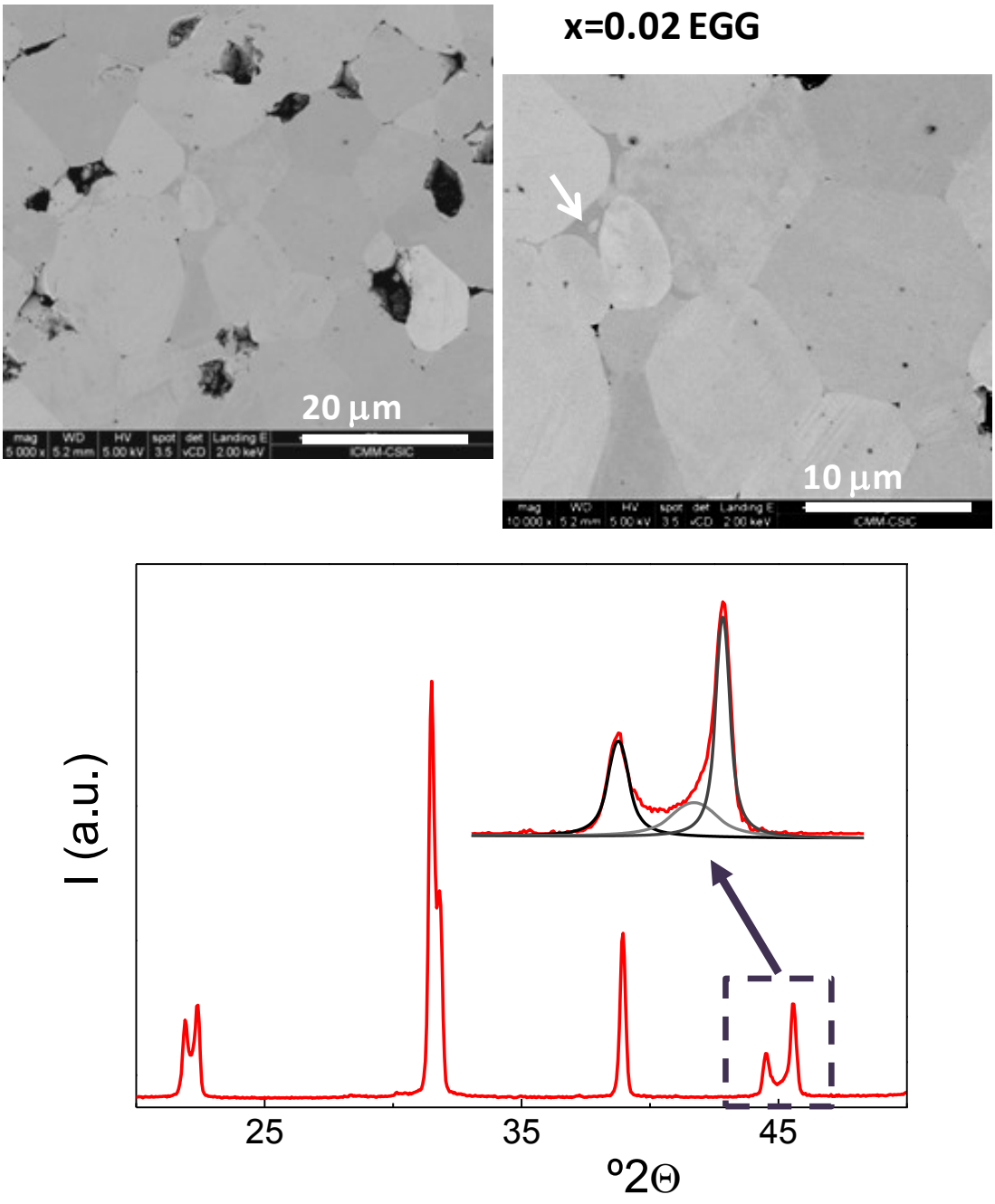

Fig. 5. SEM images and XRD pattern of a $Bi_{0.36}Pb_{0.64}Sc_{0.36-x}Mn_xTi_{0.64}O_3$ ceramic with x=0.02 and coarsened (EGG) microstructure, showing the shift of the phase coexistence towards the tetragonal side of the MPB. The arrow indicates the presence of liquid phases at treble points.

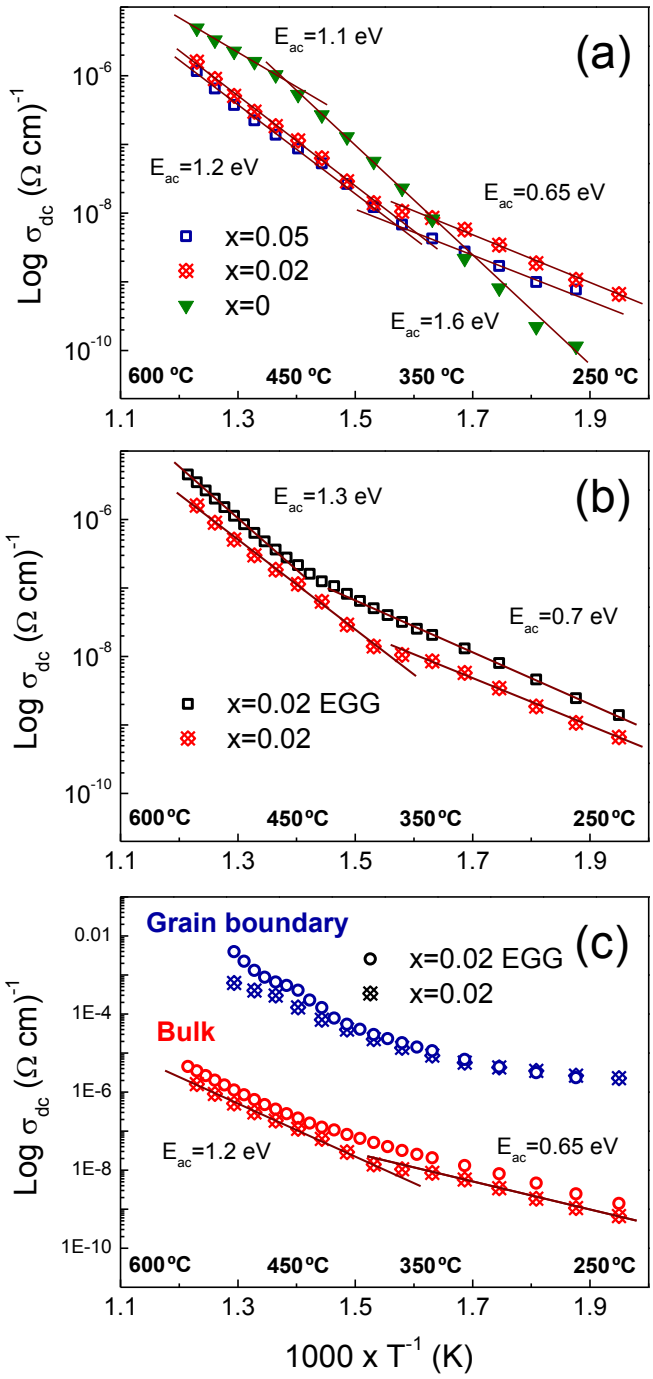

Fig. 6. Arrhenius plots of the total *dc* conductivity for $Bi_{0.36}Pb_{0.64}Sc_{0.36-x}Mn_xTi_{0.64}O_3$ ceramics with x=0, 0.02 and 0.05 (a) fine-grained and (b) after microstructure coarsening (EGG), (c) along with its bulk and grain boundary components, demonstrating the correct incorporation of the point defects (by the appearance of the low temperature electronic conduction mechanism with $E_a \approx$ 0.65 eV).

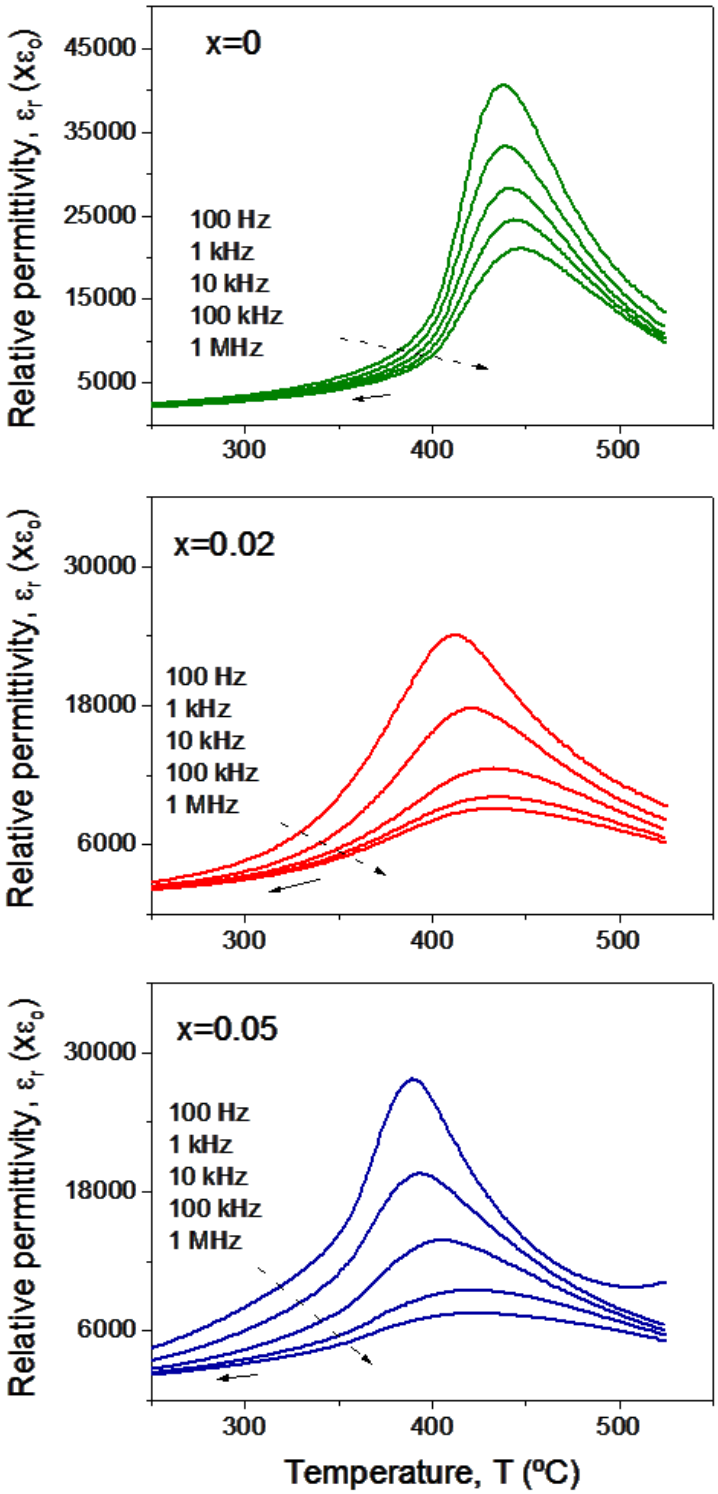

Fig. 7. Temperature dependence of the relative permittivity for the series of $Bi_{0.36}Pb_{0.64}Sc_{0.36-x}Mn_xTi_{0.64}O_3$ fine grained ceramics with x=0, 0.02 and 0.05 at several frequencies, measured on cooling.

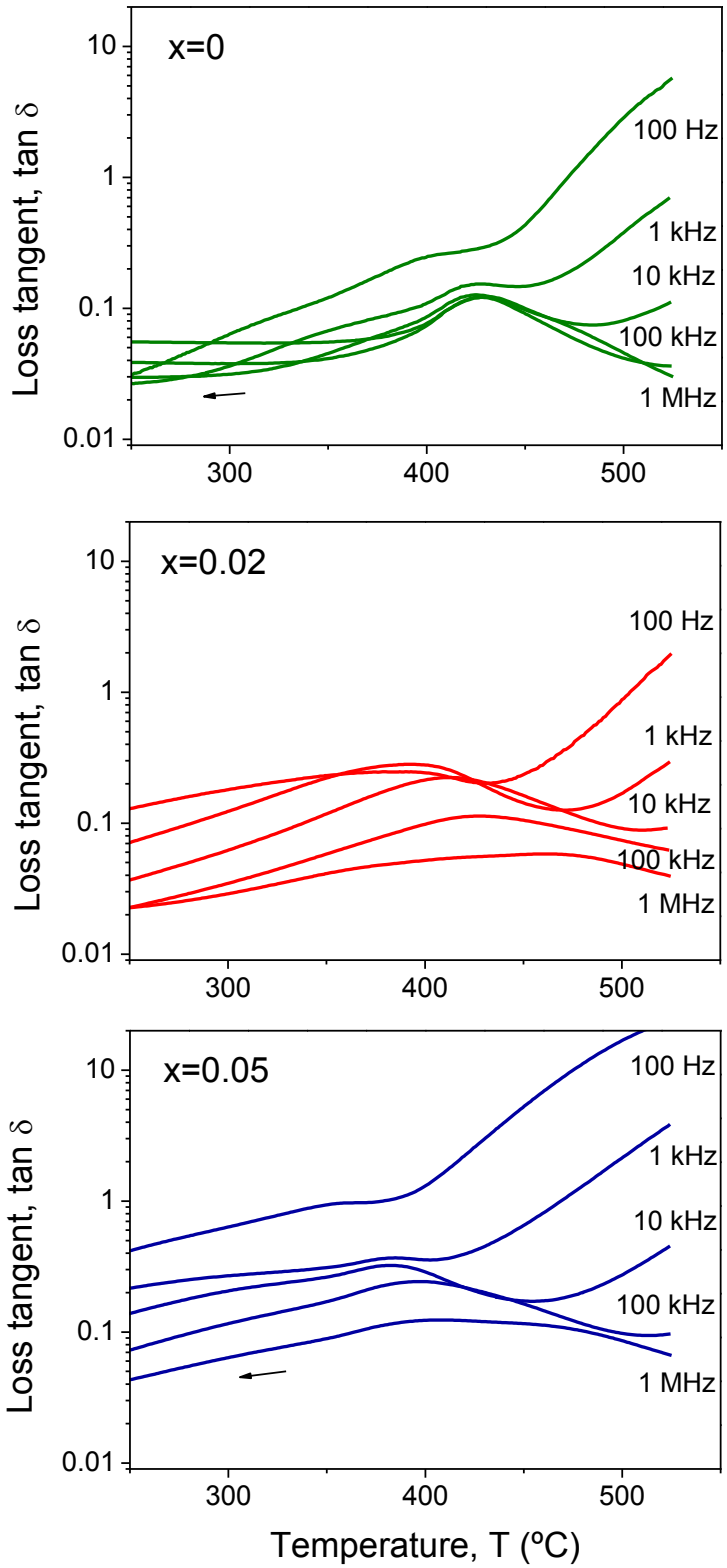

Fig. 8. Temperature dependence of the loss tangent for the series of $Bi_{0.36}Pb_{0.64}Sc_{0.36-x}Mn_xTi_{0.64}O_3$ fine grained ceramics with x=0, 0.02 and 0.05 at several frequencies, measured on cooling.

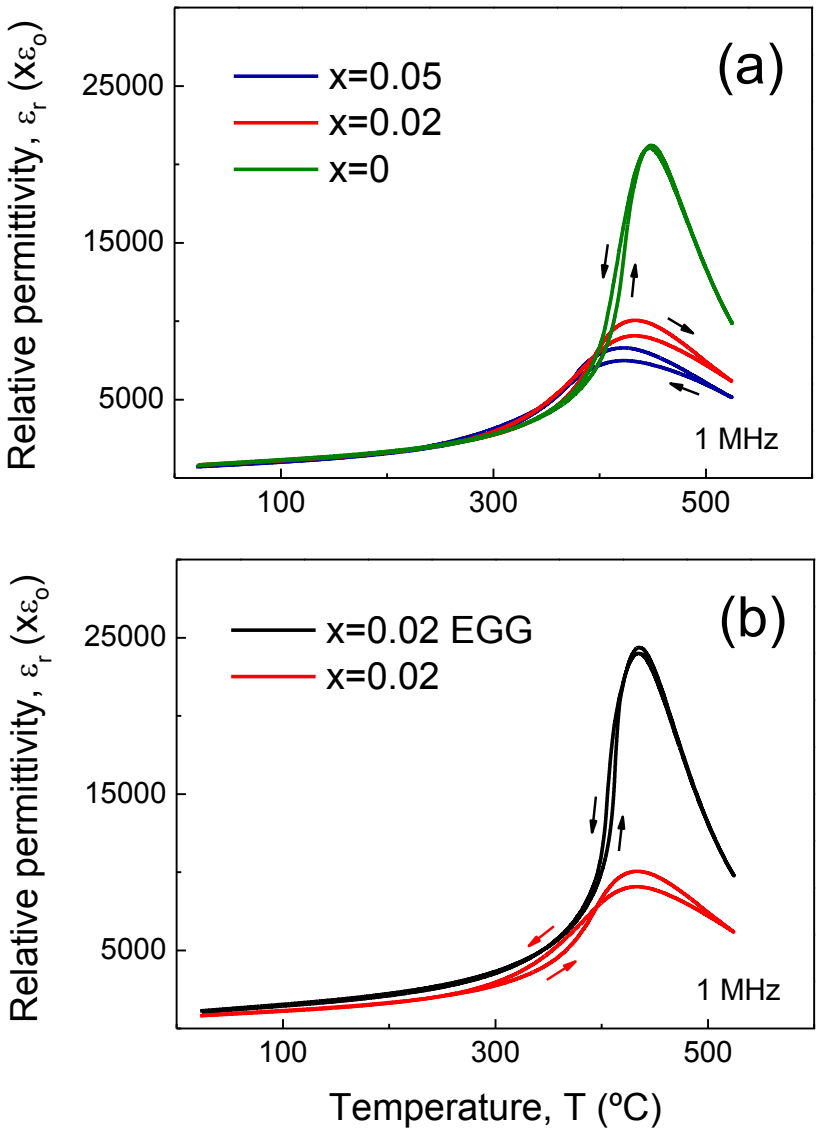

Fig. 9. Temperature dependence of the relative permittivity of $Bi_{0.36}Pb_{0.64}Sc_{0.36-x}Mn_xTi_{0.64}O_3$ ceramics with x=0, 0.02 and 0.05 (a) fine-grained and (b) after microstructure coarsening (EGG), showing the decrease of the ferroelectric transition temperature with increasing Mn.

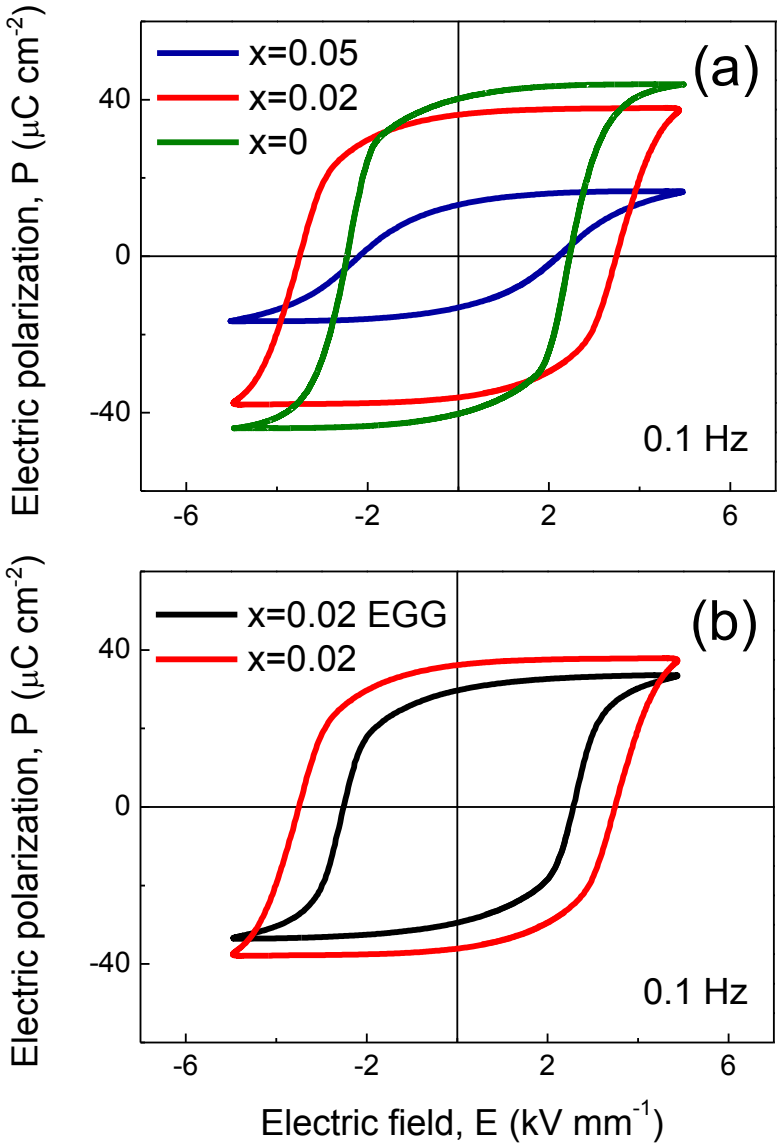

Fig. 10. Ferroelectric hysteresis loops for $Bi_{0.36}Pb_{0.64}Sc_{0.36-x}Mn_xTi_{0.64}O_3$ ceramics with x=0, 0.02 and 0.05 (a) fine-grained and (b) after microstructure coarsening (EGG), showing the effect of the point defect engineering in increasing the coercive field (and thus decreasing the domain wall mobility).

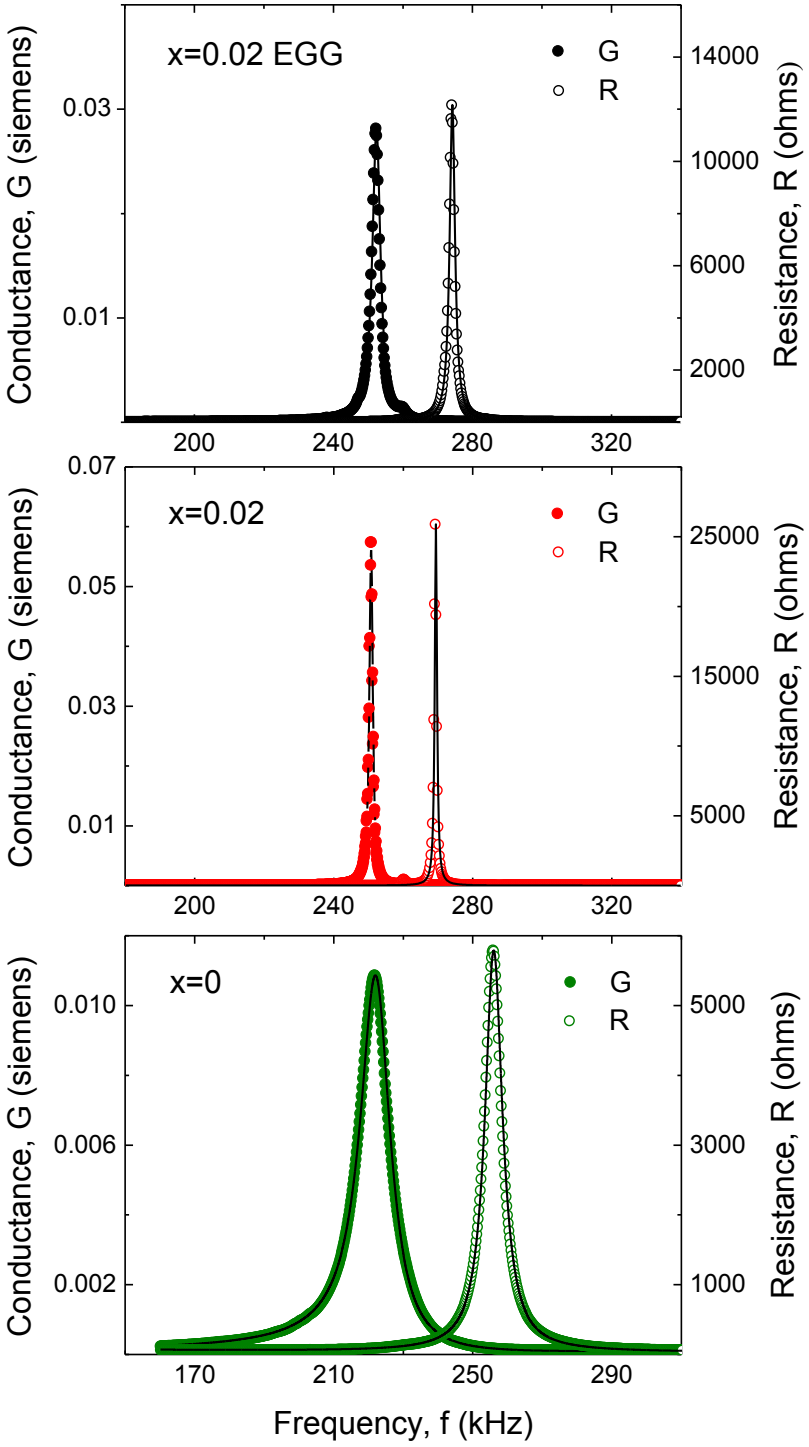

Fig. 11. Piezoelectric radial resonances for $Bi_{0.36}Pb_{0.64}Sc_{0.36-x}Mn_xTi_{0.64}O_3$ ceramics with x=0 (fine grained) and 0.02 (both fine grained and after microstructure coarsening), showing the effect of the point defect engineering in increasing the mechanical quality factor (and thus decreasing losses).